Domain-pattern transfer dynamics across an artificial magnetoelectric interface

Gabriele De Luca[1*†], Peggy Schoenherr[1], Johannes Mendil[2], Dennis Meier[3], Manfred Fiebig[1], and Morgan Trassin[1]

[1]Department of Materials, ETH Zurich, Vladimir-Prelog-Weg 4, 8093 Zürich, Switzerland
[2]Department of Materials, ETH Zurich, Hönggerbergring 64, 8093 Zürich, Switzerland
[3]Department of Materials Science and Engineering, Norwegian University of Science and Technology (NTNU), Sem Sælandsvei 12, NO-7491 Trondheim, Norway

* Current address: Department of Physics, University of Zurich, Winterthurerstrasse 190, 8057 Zürich, Switzerland

† deluca@physik.uzh.ch

Magnetoelectric interfaces provide efficient pathways for manipulating the magnetic order with low-power-consuming electric fields. A prime example for this is the voltage-controlled domain-pattern transfer from a multiferroic $BiFeO_3$ film into an amorphous $Co_{0.9}Fe_{0.1}$ ferromagnetic layer. Here we use a combination of optical second harmonic generation and magnetic force microscopy to scrutinize the dynamics of this transfer. The non-destructive nature of our analysis permits the in-operando examination of the magnetoelectric poling dynamics. We trigger ferroelectric switching events in $BiFeO_3$ and track the evolution of their magnetoelectric transfer to the ferromagnetic domains of the $Co_{0.9}Fe_{0.1}$ with spatial resolution. This reveals a wake-up effect in the magnetoelectric coupling across the interface. It is followed by simultaneous 90° rotations of the in-plane net polarization and net magnetization that progresses with the increase of the voltage applied to the device.

I. Introduction

The possibility of controlling magnetization with an electric field enables the development of electronic devices at drastically reduced energy consumption [1–4]. Multiferroic materials, in which such a magnetoelectric (ME) manipulation is achieved, experienced a resurgence of interest

during the last few years [5]. The scarcity of room-temperature ME multiferroics, i.e. materials with coexisting and coupled ferroelectric (FE) and ferromagnetic (FM) orders, encouraged research on composite multiferroic materials, in which a FM magnetostrictive and a FE piezoelectric constituent are combined in granular or layered form [6]. More controlled approaches implement the desired ME functionality at or across well-defined interfaces of heterostructures [7–9], for example employing piezoelectric substrates [10], or by directly tuning the magnetic anisotropy with an electric field [11,12] or, very recently, by atomically engineering the ferroic phases in an oxide superlattice [13].

The ultimate goal of a room-temperature electric-field-induced reversible switching of the magnetization was realized by combining multiferroic $BiFeO_3$ (BFO) with $Co_{0.9}Fe_{0.1}$ (CoFe) [14–16]. In BFO, FE and antiferromagnetic (AFM) orders are bound together [17]. A canted interfacial magnetic moment, linked one-to-one to the electric dipole moment, can drive the coupling between the AFM order and the FM order of the adjacent CoFe layer. This finally enables to control the magnetization with an electric field via a FE-to-AFM-to-FM domain-pattern transfer across the interface [14,16]. For understanding, controlling and technologically implementing this complex multi-stage ME transfer chain, we have to be able to track the dynamics of the ME poling. A feasible procedure for this operation consists in recording both the FE domain distribution in BFO and the FM domain pattern induced in the CoFe layer.

A notorious challenge, however, in investigating ferroic heterostructures consists in reaching buried properties and interfacial effects [18], like in the present case where the FE state of the BFO film is buried beneath the CoFe layer. This can be bypassed by etching away the metallic electrode [14,16], but this inevitably breaks the device functionality and impedes any further investigation of the poling procedure.

In this work, we overcome this limitation by following the ME poling dynamics of a BFO/CoFe heterostructure applying optical second harmonic generation (SHG) and magnetic force microscopy (MFM) for non-destructive probing. SHG is sensitive to the buried FE domain state and MFM to the resulting FM order. Tracking the poling dynamics reveals that, as complement to previous observations [14,15], the FE and FM order in BFO and CoFe, respectively, are initially not coupled. Instead, the clamping is activated by the first-time application of an electric field of the order of the BFO coercive field. Following this wake-up effect, we control the evolution of the FM domain distribution in the CoFe layer by adjusting the poling voltage and observe that the main effect of the poling is the generation of differently oriented stripe-domain patterns.

II. Experiment

Our multilayer is grown by pulsed laser deposition (PLD) using a stoichiometric BFO target on a $SrRuO_3$ (SRO)-buffered (110)-oriented $DyScO_3$ (DSO) substrate. The film is 50 nm thick and grows with a (001) orientation. Additional growth parameters are described elsewhere [19]. The magnetic CoFe layer and a Pt capping layer, both 3 nm thick, are sputtered in situ after the BFO deposition in order to minimize interface contamination. Finally, by optical lithography and Ar^+-ion milling, we fabricate a Pt/CoFe bilayer in the shape of a µm-sized cross. In Fig. 1, we present the characterization of our device by SHG and MFM. A sketch of the multilayer structure is included as inset of Fig. 1(a).

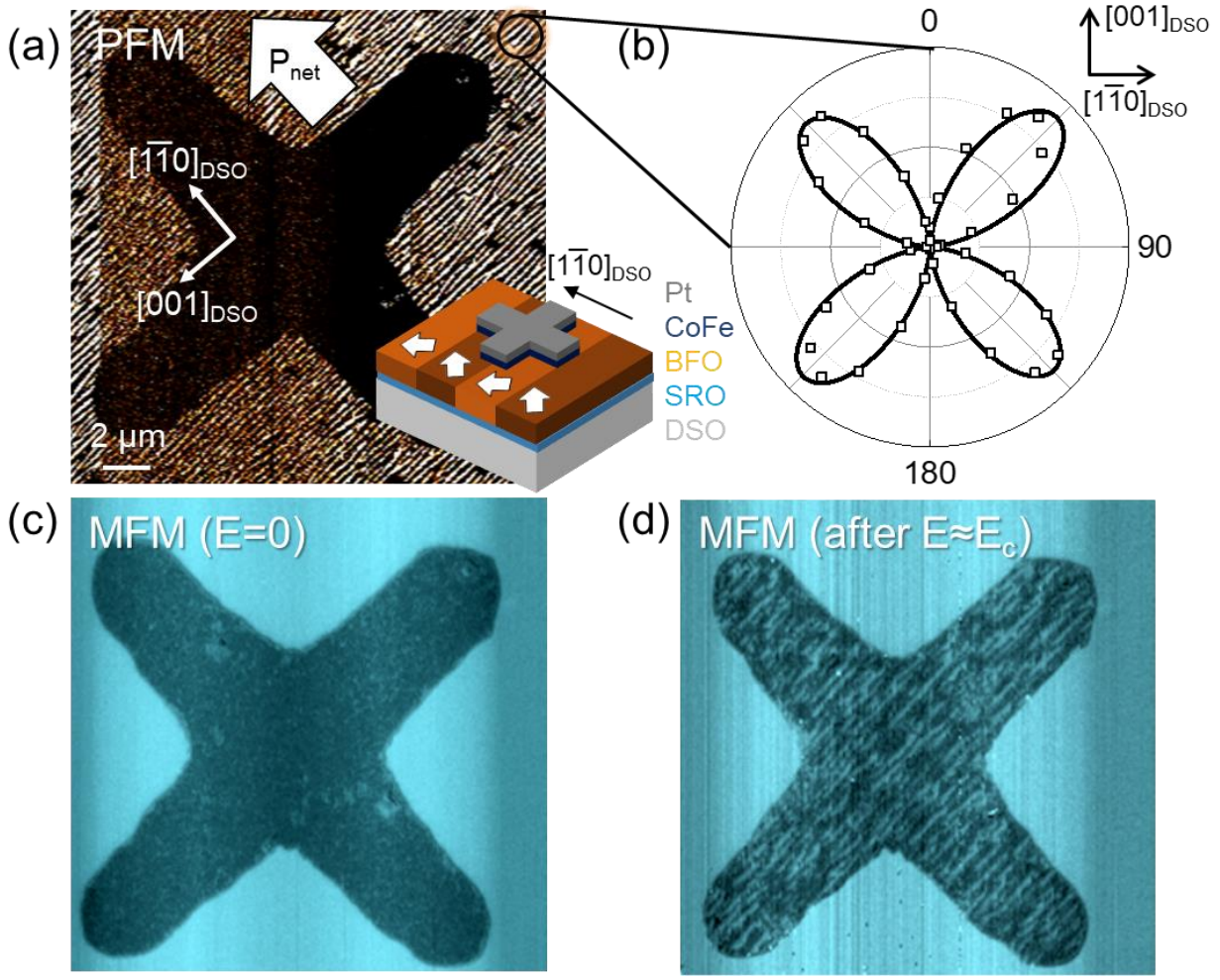

Figure 1. Magnetoelectric characterization of the Pt/CoFe/BFO/SRO//DSO heterostructure. (a,b) and (c,d) refer to the FE and FM, respectively. (a) The in-plane PFM response reveals a FE stripe-domain distribution in the BFO, yielding an in-plane net polarization P_{net} (white arrow) along $[1\bar{1}0]_{DSO}$. The cross-shaped metallic electrode prevents the observation of the buried FE BFO domain structure. In the inset, a schematic of the multilayer structure is depicted. White arrows indicate the in-plane polarization in the single stripes that sums up to P_{net} (b) SHG polarization analysis on the highlighted circular region of the BFO film in (a). The angular dependence is associated to the rotation of the polarization of the incoming light while the polarization of the outgoing SHG light is fixed parallel to $[001]_{DSO}$ (see Fig. 2(c)). Open squares and continuous lines represent collected data and SHG fit, respectively. (c) MFM performed before the first application of a poling voltage reveals uniform distribution of magnetization in the CoFe. (d) MFM performed after application of an electric poling field close to the BFO coercive field yields magnetic stripes with the same orientation as in the BFO film not covered by CoFe.

With x-ray diffraction, we verify the structural properties of our BFO film. The θ-2θ scan (not shown) exhibits fringes around the (001) peak, which corroborates the high interfacial quality of the heterostructure. Exploiting the anisotropic in-plane strain exerted by the DSO substrate, we engineer a stripe-like FE domain pattern in the BFO film [20]. This is verified by piezoresponse force microscopy (PFM) in the region not covered by the CoFe/Pt bilayer, see Fig. 1(a). When probing the region of the BFO film not covered by the electrode, the angular dependence of the $[001]_{DSO}$-polarized SHG light on the polarization of the incident fundamental light yields four equally shaped lobes (see Fig. 1(b)) [19]. This characteristic polarization dependence of a stripe-domain pattern will become useful later when discussing the domain structure of the BFO layer buried below the CoFe.

We then employ MFM to study the FM domain distribution in CoFe [15]. Surprisingly, we observe in Fig. 1(c) that in the as-grown heterostructure there is no domain imprint from the BFO film to the overlying CoFe layer. After applying an out-of-plane electric field via a scanning-probe-microscopy contact, however, we see in Fig. 1(d) that a stripe pattern similar to the buried BFO domain pattern has appeared in the CoFe. The electric field required to activate the coupling across the interface has to be close to the BFO thin film coercive field E_c (≈ 600 kV/cm in our device) [19].

The activation of the magnetic coupling (AFM to FM) with an electric field is reminiscent of the wake-up effect observed in ferroelectrics like Si:HfO, $PbZr_xTi_{1-x}O_3$ or $SrBi_2Ta_2O_9$, where a certain number of electric-field cycles beyond the coercive field are required to fully activate the switchability of the order parameter [21]. In our present case, the wake-up effect is a valuable ingredient of the ME coupling dynamics in the BFO/CoFe system. But for tracking this dynamics, we need to resolve the exact impact of the external electric field. In particular, we have to find a

way to non-destructively monitor how the ME coupling evolves with the applied electric field. For this, we have to quantify the poling of the domain distribution in the buried BFO layer. Conventional characterization techniques like PFM are not suitable here because they are limited to out-of-plane response (Fig. 1(a)) [22]. A non-destructive electron-microscope analysis, as performed in earlier work, is not feasible either because of the changes in the BFO lattice constant occurring as a result of the poling process [23].

To circumvent these limitations, we monitor the evolution of the buried BFO domain pattern under the applied electric field via the angular dependence of the spatially resolved SHG signal and we correlate it with MFM scans of the CoFe domain pattern at the same location. We do this under operating conditions so that we track the ME coupling dynamics throughout the poling process.

III. Results

A. Domain pattern evolution in BFO

SHG is sensitive to the breaking of inversion symmetry in a non-centrosymmetric material and hence ideal for probing ferroelectric order [19,24–26]. The optical frequency doubling is described by $P_i(2\omega) = \varepsilon_0 \chi_{ijk} E_j(\omega) E_k(\omega)$ with the rank-three tensor χ_{ijk} as SHG susceptibility parametrizing the light-matter interaction [24,26]. The point-group symmetry of the compound determines the allowed χ_{ijk} tensor components and the relation between them [19,27]. Our domain-engineered BFO film exhibits a stripe domain state yielding a net in-plane polarization P_{net} oriented along $[1\bar{1}0]_{DSO}$ as shown in Fig. 1(a) [20]. Because the width of the stripe domains (≈ 100 nm) is below the lateral optical resolution (≈ 1 μm), the nonlinear optical response is directly sensitive to P_{net} rather than to the polarization of the individual domains. SHG therefore distinguishes between regions with differently oriented stripe patterns without resolving individual domains [19].

To observe the evolution of the BFO domain state as a function of increasing bias voltage, we exploit the non-destructive nature of SHG. In our heterostructure, the optical penetration depth is limited by the absorption of light in the metallic electrode. For metallic layers of ≈ 10 nm, as in our case, the light is not completely absorbed [19,28]. Hence, we can track the SHG generated in the BFO layer buried beneath the CoFe. The monoclinic point group *m* of the BFO films leads to the independent χ_{ijk} tensor components χ_{xxx}, χ_{xxy}, χ_{xyy}, χ_{yyy}, χ_{yyx}, χ_{yxx}, χ_{xzz}, χ_{yzz}, χ_{zzx}, χ_{zzy}. Some of these components are known to be negligibly small which allows us to perform a simplified fit of the SHG data with a reduced number of χ_{ijk} fit parameters [19].

Figure 2 shows the SHG response measured on the area covered by the cross-shaped electrodes for different poling fields. In the left column we see the spatially resolved SHG signal of the χ_{xxx} component while in the central column we present the corresponding SHG polarization analysis of the signal gained in the area covered by the electrode. As mentioned, we rotate the polarization of the incoming light while fixing the polarization of the SHG light along $[001]_{DSO}$. A schematic of the reflection setup is provided in Fig. 2(c). In the third column, we sketch the domain pattern derived from the SHG polarization analysis with the model explained in the following. We increase the poling field row by row in order to determine its influence on the FE domain pattern.

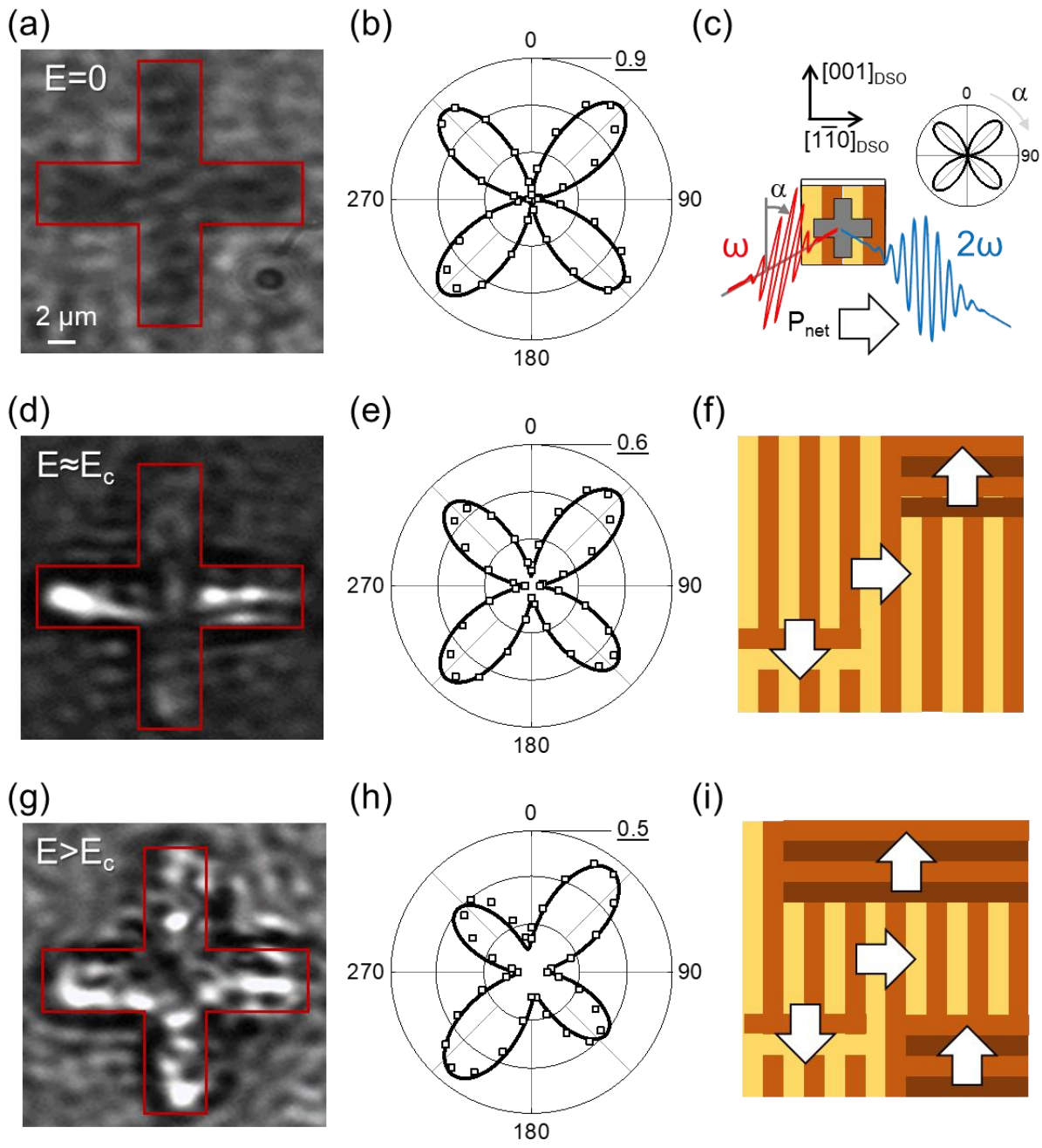

Figure 2. SHG characterization of the FE BFO layer buried beneath the CoFe. (a,d,g) Spatially-resolved SHG images of light from the χ_{xxx} component collected after application of the indicated electric field. The red contour line highlights the area of the cross-shaped CoFe layer. White blotches indicate the emergence of additional SHG contributions associated to a rotation of FE polarization. (b,e,h) SHG polarization analysis as sketched in (c) after application of the indicated electric field. Open squares and continuous lines represent collected data and SHG fit, respectively. Underlined numbers are the SHG intensity in arbitrary units. (c) Schematic of the experimental reflection geometry. (f,i) Schematic of multiferroic domain stripe distribution in the BFO after the application of an electric field $E \approx E_c$ and $E > E_c$, respectively. The white arrows indicate the local in-plane net polarization.

The first row of Fig. 2 corresponds to the pristine device already shown in Fig. 1(a). No voltage has been applied yet and by MFM we observe the absence of magnetic stripe domains in the CoFe as already shown in Fig. 1(c). Strikingly, the SHG polarization dependence in the region covered by the electrode (Fig. 2(b)) is the same as in the region not covered (Fig. 1(b)). We therefore conclude that the FE domain distribution in the buried BFO is the same as in the region not covered by CoFe, with P_{net} along $[1\bar{1}0]_{DSO}$ (Fig. 1(a)) [19,20]. This means that the room temperature sputtering of the metallic layer does not perturb the FE domain state of the underlying BFO film. The FE stripe domains are present as before but we see no evidence of the coupling into the FM layer across the interface.

The poling dynamics addressed by rows 2 and 3 of Fig. 2 can essentially have two different outcomes. Limiting our analysis to the in-plane projection of the BFO polarization, we may find [29,30]:

(i). Reversal of the in-plane net polarization of the stripe pattern ($+P_{net}^{180}$ to $-P_{net}^{180}$) while keeping the orientation of the stripes as such [31].

(ii). Nucleation of an orthogonal set of stripes along with a ±90° rotation of the in-plane net polarization (P_{net}^{180} to P_{net}^{90}) [19,30].

A partial net polarization *reversal* (i) changes the overall intensity of the SHG emission due to the destructive interference between SHG contributions from areas with $+P_{net}^{180}$ and $-P_{net}^{180}$ [32,33]. It will not lead to new, differently polarized, SHG components. The 90° net polarization *rotation* (ii), instead, leads to new SHG components resulting in a change of the angular dependence of the SHG light. As for the case (i), destructive interference between the $+P_{net}^{90}$ and $-P_{net}^{90}$ areas will reduce the overall intensity of these new contributions. So, after the poling, four possible stripe domain

patterns with four different orientations of the macroscopic net polarization ($\pm P_{net}^{180}$, $\pm P_{net}^{90}$) can in principle coexist below the electrode area [29,30].

Now we move to the second row of Fig. 2 and investigate the effect of an electric poling field close to the BFO coercive field ($E \approx E_c$). A deviation from the fourfold anisotropy of the SHG polarization dependence in Fig. 2(e) indicates the presence of new SHG components associated with a 90° rotation of the net polarization. This is also visible in the spatially resolved SHG image in Fig. 2(d) where white blotches indicate an inhomogeneous distribution of domains with $\pm P_{net}^{90}$. Although the polarization anisotropy change is small compared to the as-grown device (see Figs. 2(e) and 2(b), respectively), the quantitative analysis below will show that the SHG measurement is very sensitive to the presence of new χ_{ijk} components [19,24]. In the third row, application of a larger poling voltage (see Fig. 2(g)) results in a stronger deviation from the original polarization anisotropy (Fig. 2(h)), revealing an increase of the area yielding a 90° rotation of P_{net}.

To quantify the amount of stripe domains reoriented by the poling voltage, we fit the polarization dependence of the SHG signal in Figs. 2(b,e,h) using the SHG susceptibilities derived from Fig. 1(b) [19] and we introduce $\delta P_{net}^{\pm 180}$ and $\delta P_{net}^{\pm 90}$ as fit parameters representing the areal fractions in the sample covered by the four possible types of stripe-domain patterns introduced above [24,29]. Only three of these are independent because $\sum \delta P_{net}^{\pm(90,180)} = 1$ [24,34]. The fit values are reported in Table T1. We also explicitly report the percentage of areas with stripes oriented orthogonal ($\delta P_{net}^{90} = \delta P_{net}^{+90} + \delta P_{net}^{-90}$) to the as-grown state because these are identified by the different orientation of the domain stripes in the MFM scans discussed in the next section. There is no mixture of domains of $+P_{net}^{180}$ and $-P_{net}^{180}$ as expressed by $\delta P_{net}^{+180} = 0$ within the error of the fit. This is expected as it was established that an out-of-plane voltage will result in a full reversal of the in-plane polarization in Pt/CoFe/BFO/SRO capacitors [14,16,23]. In contrast, the 90° rotation

of the polarization leads to a distribution of regions with $+P_{net}^{90}$ and $-P_{net}^{90}$, yet still with a dominance of one direction ($+P_{net}^{90}$) over the other ($-P_{net}^{90}$), see sketch in Fig. 2(f). Hence, from the SHG analysis, we derive that before the voltage application the domain distribution in the BFO corresponds to the as-grown state, with a net in-plane polarization $+P_{net}^{180}$ pointing along $[1\bar{1}0]_{DSO}$ [14,19,20]. With an electric field intensity of $E \approx E_c$, we find $\delta P_{net}^{90} \approx 17\%$ for the stripe domains with a ±90° rotation of the P_{net}. By increasing the poling voltage, we are nucleating a larger amount of stripe domains that are polarized along $[001]_{DSO}$, orthogonal to the as-grown direction ($\delta P_{net}^{90} \approx 37\%$); see sketch in Fig. 2(i).

	SHG (values in percentage)					MFM
E Field	δP_{net}^{+180}	δP_{net}^{-180}	δP_{net}^{+90}	δP_{net}^{-90}	δP_{net}^{90}	δM_{net}^{90}
E = 0	100 ± 1	0 ± 1	0 ± 1	0 ± 1	0 ± 2	No coupling
$E \approx E_c$	1 ± 1	82 ± 1	11 ± 1	6 ± 1	17 ± 2	12 ± 5
$E > E_c$	0 ± 1	63 ± 1	34 ± 1	3 ± 1	37 ± 2	27 ± 3

Table 1. Quantification of the magnetoelectric poling dynamics. Areal fractions of the possible orientations of P_{net} and M_{net} in the BFO/CoFe system are shown for different applied electric fields. The values were derived from fits of the SHG polarization dependence in Fig. 2 (see text) and application of a k-means clustering algorithm to the MFM scans in Fig. 3. E is the electric poling field, $\delta P_{net}^{\pm 180,90}$ are the areal fractions of the four types of FE stripe-domain patterns (see text), $\delta P_{net}^{90} = \delta P_{net}^{+90} + \delta P_{net}^{-90}$ is the areal fraction of FE domain stripes in BFO oriented along $[1\bar{1}0]_{DSO}$, δM_{net}^{90} is the areal fraction of FM domain stripes in CoFe oriented along $[1\bar{1}0]_{DSO}$. Values are given in percent.

B. Magnetic domain distribution in CoFe

We use now MFM to visualize the effect the voltage-induced dynamics of the ferroelectric stripe domains in the BFO has on the magnetic domain distribution of the overlying CoFe layer. A weak in-plane magnetic field applied during the MFM scans allows to readily distinguish areas with 180° and 90° stripe-domain patterns, as we explain in the following.

When the CoFe is magnetically coupled to BFO, it shows a magnetic easy axis perpendicular to the direction of the domain stripes along the $[1\bar{1}0]_{\mathrm{DSO}}$ or $[001]_{\mathrm{DSO}}$ net in-plane polarization direction of the BFO. Hence, the coercive magnetic field $H_{\parallel} \parallel P_{net}$ needed to uniformly align the CoFe magnetization is lower than the coercive field $H_{\perp} \perp P_{net}$ [15]. By applying a field $H_{\parallel} < H < H_{\perp}$ only stripes parallel to the H direction will remain. By applying H along $[1\bar{1}0]_{\mathrm{DSO}}$ or $[001]_{\mathrm{DSO}}$ we can thus distinguish the regions with stripes along $[1\bar{1}0]_{\mathrm{DSO}}$ or $[001]_{\mathrm{DSO}}$, respectively. We find $\mu_0 H_{\parallel} < 10$ mT [35] and $\mu_0 H_{\perp} > 110$ mT and therefore choose $\mu_0 H = 50$ mT. In Fig. 3 we present the resulting MFM images in dependence of increasing electric poling field in each case for H applied along $[1\bar{1}0]_{\mathrm{DSO}}$ or $[001]_{\mathrm{DSO}}$ respectively.

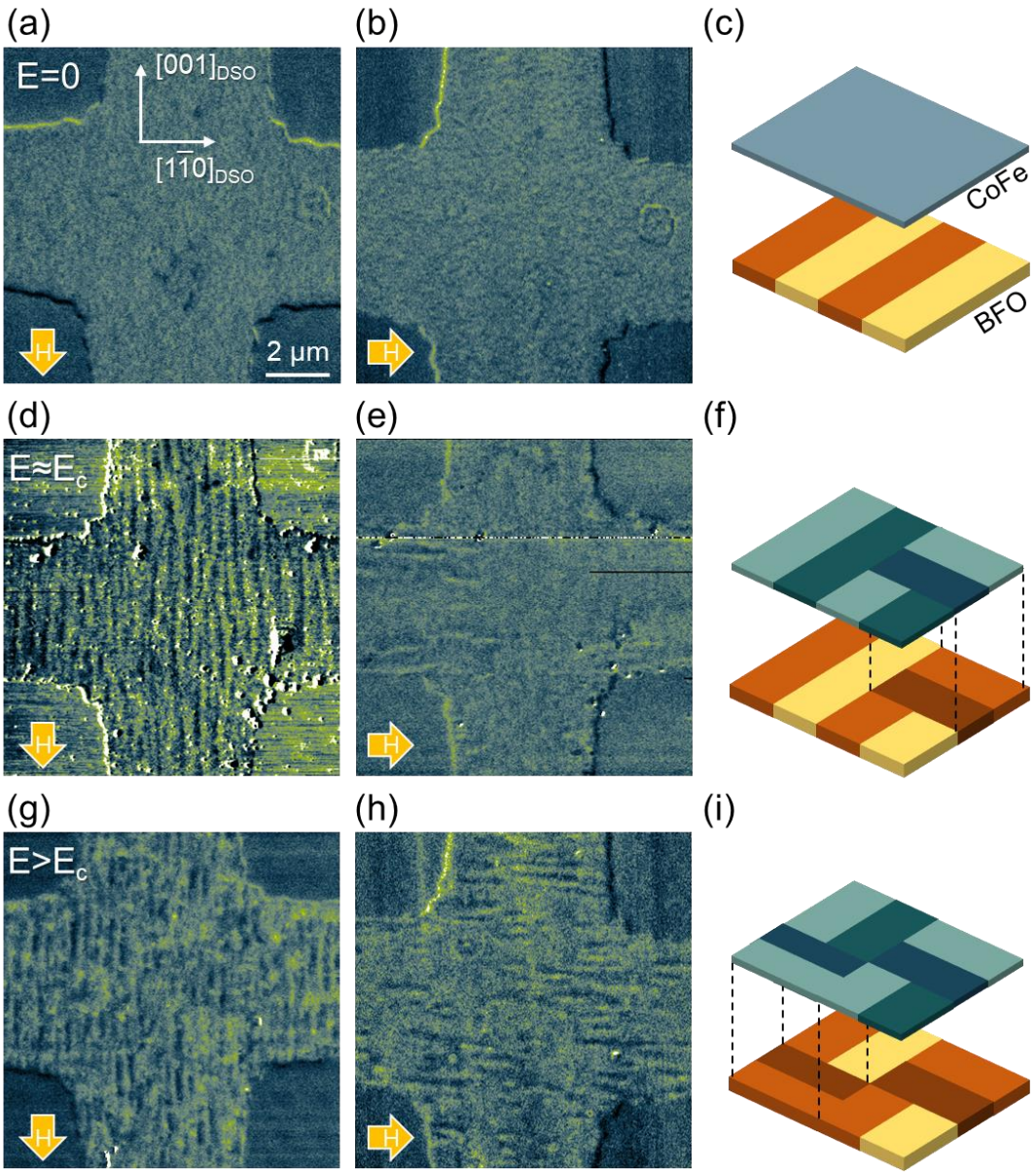

Figure 3. MFM characterization of the cross-shaped FM CoFe layer. The spatially resolved MFM scans show the magnetic domain structure of the CoFe after the application of indicated electric field. MFM scans are recorded in the presence of an in-plane magnetic field of $\mu_0 H$ = 50 mT along $[001]_{DSO}$ (a,d,g) or $[1\bar{1}0]_{DSO}$ (b,e,h), see orange arrows. (c,f,i) Schematic of the ME BFO/CoFe domain pattern transfer derived from the MFM scans. (a,b) The pristine CoFe film yields a uniform in-plane magnetization. The lack of magnetic anisotropy indicates the suppression of the ME BFO/CoFe coupling. (d,e) After application of an electric field $E \approx E_c$. The magnetic field oriented along $[001]_{DSO}$ (d) or $[1\bar{1}0]_{DSO}$ (e) filters out areas with magnetic stripe domains along $[1\bar{1}0]_{DSO}$ or $[001]_{DSO}$, respectively (see text). Stripes are mainly oriented along $[001]_{DSO}$, parallel to the as-grown buried FE domains. (g,h) Same as (d,e) after $E > E_c$. The fraction of magnetic stripes oriented along $[1\bar{1}0]_{DSO}$ has increased.

First, we discuss the case of the as-grown device. As already observed from Fig. 1(c), no magnetic stripe domains are observed. The CoFe yields uniform magnetization for H applied along both $[001]_{DSO}$ and $[1\bar{1}0]_{DSO}$ (Figs. 3(a,b)). The contrast at the edges of the cross-shaped electrode confirms that the layer is uniformly in-plane magnetized, always parallel to the direction of H. Hence, the pristine CoFe film behaves magnetically isotropically with respect to the DSO in-plane crystallographic directions, corroborating that prior to the application of an electric field there is no ME coupling between the BFO and the CoFe layer as sketched in Fig. 3(c).

The situation changes after application of an electric field $E \approx E_c$. MFM now reveals magnetic stripes with an orientation as in the underlying BFO layer, see Fig. 3(d) and also Fig. 1(d). When the in-plane magnetic field is pointing along $[001]_{DSO}$ (Fig. 3(d)) we obtain a dense pattern of stripes along $[001]_{DSO}$ all across the area covered by the electrode. In contrast, with a magnetic field along the $[1\bar{1}0]_{DSO}$ (Fig. 3(e)) we obtain an almost uniform magnetization with only a few orthogonal stripes. Thus, the distribution of domain stripes in the ferromagnetic CoFe film matches that in the ferroelectric BFO film: The magnetoelectric transfer of the net polarization to the net magnetization is now active [14–16,23] (Fig. 3(f)). Note that the activation of this transfer requires an electric field close to the BFO coercive field, indicated by the beginning 90° rotation of the BFO stripe domains. After applying a larger bias voltage, the magnetic stripes become more equally distributed between the $[001]_{DSO}$ and $[1\bar{1}0]_{DSO}$ directions (Figs. 3(g,h)). The higher field promotes the 90° rotation of the BFO stripe domains, coupled to the 90° rotation of the CoFe stripe domains.

We quantify the areal distribution of the magnetic stripes using a k-means clustering algorithm [36] with the results listed in the δM_{net}^{90} column of the Table 1. We obtain $\delta P_{net}^{90} \approx 12\%$ for $E \approx E_c$ and $\delta P_{net}^{90} \approx 27\%$ for $E > E_c$. This is in reasonable agreement with the SHG data (δP_{net}^{90}). The small difference that we observe is most likely related to the incoherent, that is, non-interfering

contributions to the SHG yield that are caused by the limited spatial coherence of our laser beam. These were not included in the fit of $\delta P_{net}^{\pm(90,180)}$, an approximation introducing a small systematic error in the SHG fits [24].

IV. Summary

In summary, using optical SHG and MFM as nondestructive in-operando probes, we track the ME coupling dynamics in a BFO/CoFe heterostructure under applied electric fields. With the SHG analysis we precisely quantify the FE domain distribution of the buried BFO buried below the metallic electrode as a function of the increasing bias voltage. MFM provides the complementary FM domain structure in the CoFe. Strikingly, we find that the interfacial coupling between the FE BFO and the FM CoFe needs to be activated by an initial applied electric field on the order of the coercive field. Clarification of the origin of this wake-up effect will require detailed future studies on strain, magnetic anisotropy, interface chemistry and higher-order magnetoelectric coupling effects. Once the BFO coercive field is exceeded, we observe nucleation of an orthogonal set of stripes with a ±90° rotation of the in-plane net polarization. The areal fraction of these orthogonal stripes scales with the applied electric poling voltage.

Thus, our in-operando access to the ME switching dynamics, enabled by noninvasive probing of the FE and FM order provides access to the reversible ME BFO/CoFe coupling dynamics with an unprecedented degree of detail. The in-operando access to the ME dynamics is also the first step towards the observation of the room-temperature reversible switching dynamics down to the ultrafast time scale, an important prerequisite for device applications.

Acknowledgments

The authors thank Ramamoorthy Ramesh, UC Berkeley, for valuable discussion. This research was supported by the EU European Research Council (Advanced Grant 694955—INSEETO).

Author contributions

All authors discussed the result and contributed to the completion of the manuscript. G. D. L. performed the SHG measurement and developed the SHG fitting model. M. T. performed the multiferroic heterostructure growth. J. M. carried out the optical lithography and ion milling. M. T., P. S. and G. D. L. performed the PFM and MFM analysis under electric and magnetic field. D. M., M. F. and M. T. designed the experiment and supervised the work.

References

[1] J. F. Scott, Nat. Mater. **6**, 256 (2007).

[2] M. Bibes and A. Barthélémy, Nat. Mater. **7**, 425 (2008).

[3] M. Bibes, J. E. Villegas, and A. Barthélémy, Adv. Phys. **60**, 5 (2011).

[4] M. Trassin, J. Phys. Condens. Matter **28**, 033001 (2016).

[5] M. Fiebig, T. Lottermoser, D. Meier, and M. Trassin, Nat. Rev. Mater. **1**, 16046 (2016).

[6] C.-W. Nan, M. I. Bichurin, S. Dong, D. Viehland, and G. Srinivasan, J. Appl. Phys. **103**, 031101 (2008).

[7] C. A. F. Vaz, J. Phys. Condens. Matter **24**, 333201 (2012).

[8] F. Matsukura, Y. Tokura, and H. Ohno, Nat. Nanotechnol. **10**, 209 (2015).

[9] J.-M. Hu, L.-Q. Chen, and C.-W. Nan, Adv. Mater. **28**, 15 (2016).

[10] C. Thiele, K. Dörr, O. Bilani, J. Rödel, and L. Schultz, Phys. Rev. B **75**, 054408 (2007).

[11] D. Chiba, M. Sawicki, Y. Nishitani, Y. Nakatani, F. Matsukura, and H. Ohno, Nature **455**, 515 (2008).

[12] T. Maruyama, Y. Shiota, T. Nozaki, K. Ohta, N. Toda, M. Mizuguchi, A. A. Tulapurkar, T. Shinjo, M. Shiraishi, S. Mizukami, Y. Ando, and Y. Suzuki, Nat. Nanotechnol. **4**, 158 (2009).

[13] J. A. Mundy, C. M. Brooks, M. E. Holtz, J. A. Moyer, H. Das, A. F. Rébola, J. T. Heron, J. D. Clarkson, S. M. Disseler, Z. Liu, A. Farhan, R. Held, R. Hovden, E. Padgett, Q. Mao, H. Paik, R. Misra, L. F. Kourkoutis, E. Arenholz, A. Scholl, J. A. Borchers, W. D. Ratcliff, R. Ramesh, C. J. Fennie, P. Schiffer, D. A. Muller, and D. G. Schlom, Nature **537**, 523 (2016).

[14] J. T. Heron, M. Trassin, K. Ashraf, M. Gajek, Q. He, S. Y. Yang, D. E. Nikonov, Y.-H. Chu, S. Salahuddin, and R. Ramesh, Phys. Rev. Lett. **107**, 217202 (2011).

[15] M. Trassin, J. D. Clarkson, S. R. Bowden, J. Liu, J. T. Heron, R. J. Paull, E. Arenholz, D. T. Pierce, and J. Unguris, Phys. Rev. B **87**, 134426 (2013).

[16] J. T. Heron, J. L. Bosse, Q. He, Y. Gao, M. Trassin, L. Ye, J. D. Clarkson, C. Wang, J. Liu, S. Salahuddin, D. C. Ralph, D. G. Schlom, J. Íñiguez, B. D. Huey, and R. Ramesh, Nature **516**, 370 (2014).

[17] T. Zhao, A. Scholl, F. Zavaliche, K. Lee, M. Barry, A. Doran, M. P. Cruz, Y. H. Chu, C. Ederer, N. a Spaldin, R. R. Das, D. M. Kim, S. H. Baek, C. B. Eom, and R. Ramesh, Nat. Mater. **5**, 823 (2006).

[18] G. De Luca, M. D. Rossell, J. Schaab, N. Viart, M. Fiebig, and M. Trassin, Adv. Mater. **29**, 1605145 (2017).

[19] M. Trassin, G. De Luca, S. Manz, and M. Fiebig, Adv. Mater. **27**, 4871 (2015).

[20] Y.-H. Chu, Q. He, C.-H. Yang, P. Yu, L. W. Martin, P. Shafer, and R. Ramesh, Nano Lett.

9, 1726 (2009).

[21] D. Zhou, J. Xu, Q. Li, Y. Guan, F. Cao, X. Dong, J. Müller, T. Schenk, and U. Schröder, Appl. Phys. Lett. **103**, 192904 (2013).

[22] S. V. Kalinin, B. J. Rodriguez, S.-H. Kim, S.-K. Hong, A. Gruverman, and E. A. Eliseev, Appl. Phys. Lett. **92**, 152906 (2008).

[23] J. Unguris, S. R. Bowden, D. T. Pierce, M. Trassin, R. Ramesh, S.-W. Cheong, S. Fackler, and I. Takeuchi, APL Mater. **2**, 076109 (2014).

[24] S. A. Denev, T. T. A. Lummen, E. Barnes, A. Kumar, and V. Gopalan, J. Am. Ceram. Soc. **94**, 2699 (2011).

[25] A. Kumar, S. Denev, R. J. Zeches, E. Vlahos, N. J. Podraza, A. Melville, D. G. Schlom, R. Ramesh, and V. Gopalan, Appl. Phys. Lett. **97**, 112903 (2010).

[26] J. Nordlander, G. De Luca, N. Strkalj, M. Fiebig, and M. Trassin, Appl. Sci. **8**, 570 (2018).

[27] D. Fröhlich, T. Kiefer, S. Leute, and T. Lottermoser, Appl. Phys. B Lasers Opt. **68**, 465 (1999).

[28] Z. Q. Qiu and S. D. Bader, J. Magn. Magn. Mater. **200**, 664 (1999).

[29] S. K. Streiffer, C. B. Parker, a E. Romanov, M. J. Lefevre, L. Zhao, J. S. Speck, W. Pompe, C. M. Foster, and G. R. Bai, J. Appl. Phys. **83**, 2742 (1998).

[30] N. Balke, S. Choudhury, S. Jesse, M. Huijben, Y. H. Chu, A. P. Baddorf, L. Q. Chen, R. Ramesh, and S. V. Kalinin, Nat. Nanotechnol. **4**, 868 (2009).

[31] S. H. Baek, H. W. Jang, C. M. Folkman, Y. L. Li, B. Winchester, J. X. Zhang, Q. He, Y. H. Chu, C. T. Nelson, M. S. Rzchowski, X. Q. Pan, R. Ramesh, L. Q. Chen, and C. B. Eom, Nat. Mater. **9**, 309 (2010).

[32] J. Kaneshiro, Y. Uesu, and T. Fukui, J. Opt. Soc. Am. B **27**, 888 (2010).

[33] G. De Luca, N. Strkalj, S. Manz, C. Bouillet, M. Fiebig, and M. Trassin, Nat. Commun. **8**, 1419 (2017).

[34] Y. Barad, J. Lettieri, C. D. Theis, D. G. Schlom, V. Gopalan, J. C. Jiang, and X. Q. Pan, J. Appl. Phys. **89**, 1387 (2001).

[35] L. You, B. Wang, X. Zou, Z. S. Lim, Y. Zhou, H. Ding, L. Chen, and J. Wang, Phys. Rev. B **88**, 184426 (2013).

[36] J. A. Hartigan and M. A. Wong, Appl. Stat. **28**, 100 (1979).